Surface nanostructuring of TiO_2 thin films by high energy ion irradiation

P. Romero-Gomez,[1] A. Palmero,[1,*] T. Ben,[2] J. G. Lozano,[2] S. I. Molina,[2] and A. R. González-Elipe[1]
[1]*Instituto de Ciencia de Materiales de Sevilla, CSIC/Universidad de Sevilla, c/Américo Vespucio 49, 41092 Sevilla, Spain*
[2]*Departamento de Ciencia de los Materiales e I.M. y Q.I., Facultad de Ciencias, Universidad de Cádiz, Campus Río San Pedro, s/n, Puerto Real, 11510 Cádiz, Spain*
(Received 16 March 2010; revised manuscript received 9 July 2010; published 10 September 2010)

The effects of a high ion dose irradiation on TiO_2 thin films under different conditions of temperature and ion nature are discussed. We have shown that anatase TiO_2 thin films irradiated with N^+ ions at room temperature develop a typical microstructure with mounds and voids open to the surface whereas irradiations at 700 K generate a surface pattern of well-ordered nanorods aligned with the ion beam. The formation of these patterns is caused by the simultaneous effect of ion irradiation near the film surface and a film temperature favoring the structural mobilization of the defective network of the material. To explain these phenomena, a qualitative model has been proposed and further tested by irradiating the TiO_2 thin films with F^+ and S^+ ions under different conditions. The obtained results demonstrate that ion irradiation techniques enable the formation of tilted nanorod surface patterns with lengths of about 100 nm on anatase TiO_2 thin films.

DOI: 10.1103/PhysRevB.82.115420 PACS number(s): 68.55.−a

I. INTRODUCTION

Titanium dioxide (TiO_2) is a wideband semiconductor with numerous applications in science and technology. Its excellent optical transmittance, high refractive index, and chemical stability make this material good candidate for antireflection coatings, solar cells, capacitor for high bit DRAM (dynamic random access memory), anodic electrochromic materials, etc.[1–4] Furthermore, photoactive properties of this oxide under light irradiation has fostered new and interesting applications in the field of photocatalysis, self-cleaning materials or photovoltaic cells, all of them actively investigated during the last years.[5] For these applications, it was found that the anatase crystalline phase is especially adequate to optimize many of the previous properties, and that its performance clearly improves when the film surface is nanostructured[6] and/or when it is doped with nitrogen to shift its spectral response from the ultraviolet toward the visible light spectrum.[7,8]

The development of reliable techniques for surface nanostructuring of thin films is nowadays a key issue that has been approached by different physical and chemical methods.[9] In particular, considerable efforts have been devoted during the last years to the preparation of mesostructured[10] and one-dimensional TiO_2 structures (nanorods, nanowires, and nanotubes)[11,12] which have depicted unprecedented results as hydrogen sensors, self-cleaning surfaces under ultraviolet light exposure, or dye sensitized heterojunction solar cells.[13–15] In this latter case, the presence of highly ordered one-dimensional TiO_2 arrays improves the photogenated charge carrier lifetimes by more than one order of magnitude in comparison with nanoparticulate systems (see, for instance, Ref. 16 and references therein).

In a recent publication, we showed that anatase TiO_2 thin films under the irradiation of a high energy ion beam caused important structural and chemical changes in the material, such as the decrease in crystallinity of the films and the depletion of oxygen in the upmost surface layers due to its preferential sputtering.[17] Although these phenomena have extensively been reported in the literature for this oxide material subjected to different thermal and ion-beam treatments (see, for instance, Ref. 18 and references therein), in Ref. 17 we also showed the existence of additional processes affecting the nanostructure and surface topography. For instance, we found that when a TiO_2 anatase thin film was irradiated at room temperature with a high dose of N^+ ions, with energies around 50 keV, a porous layer appeared at a depth similar to the ion projected range (R_p). Furthermore, by reducing the ion irradiation energy, and thus R_p, various surface morphologies were obtained, such as cellular defect structures or nanorods surface patterns aligned with the angle of incidence of the beam. These results suggested a strong link between pore formation mechanisms in the material and the development of nanorods at the surface. An interesting aspect of this proposed technique in comparison with other methods is the possible customization of the nanorod surface patterns. In Refs. 19 and 20, for instance, a technique that involves a femtosecond laser irradiation of the film in water was proposed. As a result, a nanorod surface pattern consisting of quasiperiodic sharp conical spikes, about 50 nm wide and with length in the micrometer range, perpendicular to the substrate, was found. These results, together with those in Ref. 17, suggest that by tuning the operational parameters, the size, length, and tilt angle of the nanorods could be controlled while further research must be carried out in order to understand the surface nanostructuring of thin films.

The formation of pores after ion irradiation has been recently reported for crystalline silicon irradiated with helium ions.[21] In this case, the very small momentum transferred during the collision, as well as the low solubility of the implanted species in the material, produced many localized point defects in the network that formed pores in the bulk of the material through segregation and precipitation mechanisms.[21] Pore formation after ion irradiation has also been intensively studied for GaN thin films,[22–24] where a stoichiometric imbalance of N and Ga in the network induced the formation of multiple N_2 molecules that, scattered in the material, generate the pores. Similar results were also obtained for materials such as Ge, GaSb, or InSb, where the

TABLE I. Irradiation conditions for each sample along with the measured resistivity of the films.

Sample	Ion	Dose (ion/cm^2)	Flux (ion/cm^2 s)	Energy (keV)	Angle (deg)	R_p (nm)	T (K)	Resistivity (Ω cm)
#1	N^+	2.4×10^{17}	2.0×10^{13}	60	45	~100	RT	3.20
#2	O^+	2.4×10^{17}	2.0×10^{13}	65	45	~100	RT	0.83
#3	N^+	2.4×10^{17}	2.6×10^{13}	15	45	~50	RT	1.90
#4	N^+	2.4×10^{17}	2.0×10^{13}	15	45	~50	700	0.078
#5	F^+	2.4×10^{17}	1.3×10^{13}	50	45	~50	RT	180
#6	F^+	2.4×10^{17}	1.3×10^{13}	50	45	~50	700	0.019
#7	S^+	5×10^{16}	1.3×10^{13}	45	45	~50	700	0.005

long-range migration of atoms through the bulk and the short-range movement of point defects during irradiation were responsible for the so-called anomalous swelling and the formation of pores.[25–27] In our previous work, we tentatively proposed that this latter mechanism could be responsible for the formation of pores in the TiO_2 thin films since they also develop when the material is irradiated with boron or sulfur, two elements that in no way could form gaseous molecules within the material. In the present work, we present a more thorough and detailed study of the changes occurring in TiO_2 thin films after irradiation under several conditions. The obtained results have enabled us to propose a general mechanism accounting for the formation of either pores in the interior of TiO_2 or ordered nanorods at its surface, depending on the conditions of the experiment. We think that the proposed model can be extended to account for the formation of voids in other oxides where generation of point and other structural defects are particularly favored. Another outcome of this investigation is the demonstration that, by fine tuning of the experimental conditions, it is possible to tailor the generation of ordered nanorod patterns on the surface of ion-beam irradiated oxides.

II. EXPERIMENTAL

TiO_2 thin films with a thickness comprised between 300 and 500 nm were deposited at 523 K using the plasma-enhanced chemical vapor deposition technique. The films, depicting the anatase structure, showed a high degree of crystallinity and a clear columnar microstructure perpendicular to the substrate. The details of the as-deposited material, as well as the description of the deposition technique, appear in Ref. 28. The ion irradiations were carried out at the Institute of Ion Beam Physics and Materials Research (Forschungszentrum Dresden-Rossendorf, Germany) under the conditions that appear in Table I. It is worth noting that in the cases where the ion irradiation was carried out at room temperature, the ion current was specifically set low enough to keep the film temperature below 70 °C (340 K). Other irradiation experiments were carried out at 700 K, a temperature at which no excessive oxygen depletion in the material due to desorption from the film surface is expected. Finally, the value of R_p was estimated through the SRIM software.[29] From now forth we will refer to each irradiation condition with the corresponding label "#" defined in Table I which, to provide a better reading of the paper, is accompanied by the following data: value of R_p, ion used for the irradiation and value of the film temperature.

Films were characterized by x-ray diffraction (XRD) in a Siemens D5000 Spectrometer working in the Bragg-Brentano configuration and using the Cu $K\alpha$ radiation as excitation source. Cross-sectional and top view scanning electron microscopy (SEM) micrographs were obtained using a Hitachi S5200 field emission microscope working at 5.0 keV for thin films grown on a silicon wafer. X-ray photoelectron spectroscopy spectra of the films were recorded in an ESCALAB 210 spectrometer working under energy transmission constant conditions. The Mg $K\alpha$ line was used for excitation spectra. They were calibrated in binding energy by referencing to the C 1s peak taken at 284.6 eV. Quantification was done by calculating the area of the peaks and by correcting these areas with the sensitivity factor of each element/electronic level. The transmittance spectra of the samples were determined by UV-vis (ultraviolet-visible) absorption spectroscopy (Perkin-Elmer Lambda 12 Spectrometer) for samples prepared on fused silica. Measurement of the surface electrical conductivity of the samples was done by using the four-point probe test. A Keithley 617 electrometer and a Hewlett-Packard 34401 A voltammeter were used for the measurements. These consisted of applying a voltage ranging between −0.25 and 0.25 V to the two external probe electrodes. The intensity was then measured within the two internal probes. High angle annular dark-field scanning transmission electron microscopy (HAADF-STEM) and electron energy loss spectroscopy (EELS) studies were carried out at 200 KV in a JEOL 2010F microscope equipped with a GIF (Gatan Imaging Filter) camera providing an energy resolution of about 1.6 eV, with a collection angle of 24 mrad.

III. RESULTS AND DISCUSSION

A. N^+ and O^+ ion beam bombardment

In Fig. 1(a), we show the cross-sectional view of a SEM micrograph taken for sample #1 (100-N^+-RT). Here, N^+ ions are implanted far from the surface, a process that in agreement with Ref. 17 results in both the formation of a porous layer at a depth about R_p and pore diameters comprised between 5 and 10 nm, and in the removal of the intrinsic co-

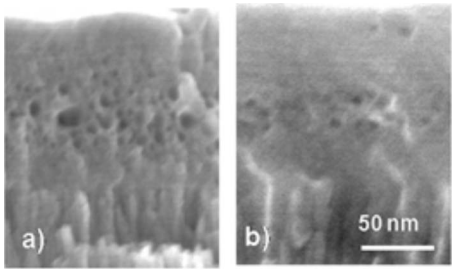

FIG. 1. Cross-sectional SEM micrographs of irradiated anatase thin films: (a) sample #1 (100-N^+-RT) in Table I and (b) sample #2 (100-O^+-RT) in Table I.

lumnar structure within the implanted region. The thickness of the sputtered region removed from the film due to the ion irradiation is estimated to be around 30–40 nm. In Fig. 1(b), we show the cross-sectional SEM image of sample #2 (100-O^+-RT). In this case, we have used O^+ instead of N^+ ions and an ion energy chosen to have a penetration depth similar to that in sample #1 (100-N^+-RT). Again, it seems clear that a porous layer appears in the material at about the same ion penetration depth, although this time the concentration and size of the pores are appreciably smaller. The columnar structure was also removed in the implantation region where, in addition to the pores, a glassy homogenous layer was formed. Regarding the similar microstructural modifications observed in Figs. 1(a) and 1(b), it is possible to conclude that pore formation is controlled by similar mechanisms in both cases, no matter whether the irradiation is done using N^+ or O^+ ions. Furthermore, surface conductivity measurements of samples #1 (100-N^+-RT) and #2 (100-O^+-RT), reported in Table I, indicate that in both cases ion bombardment has induced a considerable concentration of free electrons in the conduction band that must be associated to the formation of oxygen vacancies and Ti^{3+} species in the lattice.[30]

In Fig. 2(a), we show the top view SEM micrograph of a TiO_2 anatase thin film irradiated at room temperature with

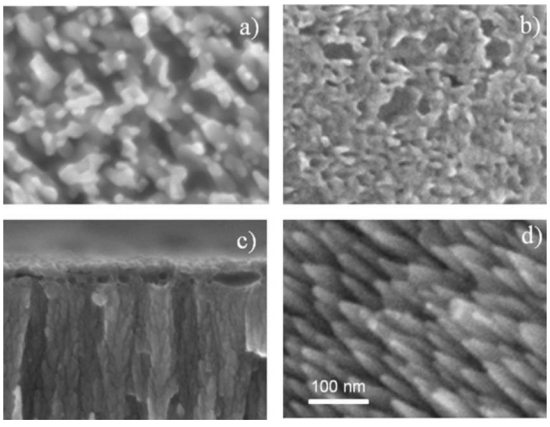

FIG. 2. SEM micrographs of irradiated anatase thin films: (a) top view of sample #3 (50-N^+-RT) in Table I and (b) top view of sample #3 (50-N^+-RT) after its annealing at 700 K, and (c) cross-sectional image of sample #3 (50-N^+-RT) after its annealing at 700 K, and (d) top view of sample #4 (50-N^+-700) in Table I.

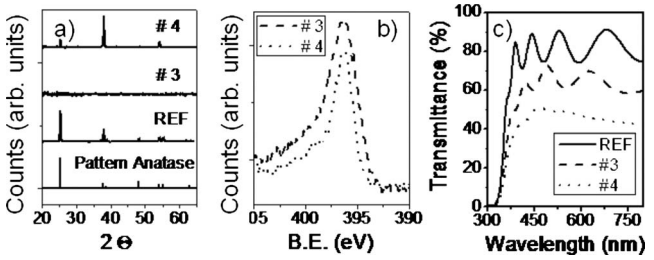

FIG. 3. Characterization results of samples #3 (50-N^+-RT) and #4 (50-N^+-700) in Table I: (a) X-ray diffraction diagrams of an as-deposited TiO_2 thin film along with those of samples #3 (50-N^+-RT) and #4 (50-N^+-700) in Table I, and a reference spectrum. (b) N 1*s* photoemission spectra of samples #3 (50-N^+-RT) and #4 (50-N^+-700), and (c) transmission spectra of samples #3 (50-N^+-RT) and #4 (50-N^+-700) along with that of a reference sample.

N^+ ions which, according to the SRIM calculations, are implanted near the surface [sample #3, (50-N^+-RT)]. This micrograph displays a surface with irregular motives and open pores. In Figs. 2(b) and 2(c), we show the top and cross-sectional SEM micrographs of the same sample annealed at 700 K after its irradiation. Comparing Figs. 2(b) and 2(c) with Fig. 2(a), we find that the annealing process induces the opening of some voids buried near the surface, thus leading to the formation of a porous surface. In parallel, voids located deeper into the material remain closed but change their shape, appearing now as large ellipsoidal voids [Fig. 2(c)]. It is likely that these large and not-spherical voids are caused by the merging of nearby smaller voids located underneath the surface. In Fig. 2(d), we depict the top SEM view of sample #4 (50-N^+-700): now the irradiation conditions are equal to those of sample #3 but imposing a film temperature of 700 K *during the irradiation*. In this case, the surface topography, quite different to that depicted in Figs. 2(a) and 2(b), is characterized by a homogenous surface pattern made of nanorods of 20–30 nm diameter aligned with the angle of incidence of the ion beam. This result suggests that the obtained morphology in Fig. 2(d) is the consequence of the *simultaneous* action of both, the ion irradiation and some thermally activated processes.

B. Structural and chemical characterization of the implanted layer

Due to the relevance of irradiations under conditions #3 (50-N^+-RT) and #4 (50-N^+-700) in relation with the formation of surface patterns, we have studied the structural and chemical modifications induced in the samples after their irradiation with nitrogen. In Fig. 3(a), we show the XRD diagram of both samples along with some reference data. The label "REF" in Fig. 3(a) corresponds to an as-deposited nonirradiated sample and the corresponding diagram depicts the typical peaks and intensities of randomly oriented TiO_2 anatase in powder form ["pattern anatase" labeled curve in Fig. 3(a)]. Furthermore, sample #3 (50-N^+-RT) depicts no clear diffraction peak, a feature that indicates a significant structural damage of the material and the loss of crystallinity.

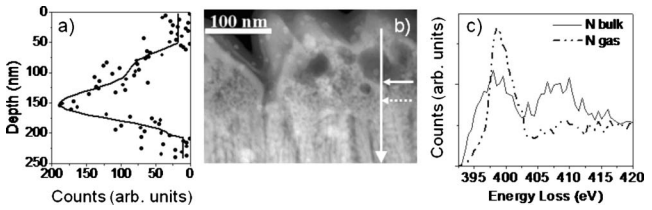

FIG. 4. Chemical analysis of sample #3 (50-N^+-RT) in Table I. (a) Nitrogen intensity profiles obtained through the EELS spectra, (b) cross-sectional HAADF image of the surface scaled with part (a), and (c) EELS spectra for the positions given by the horizontal arrows in (b) (slashed and continuum curves correspond to the slashed and continuum arrows).

Finally, sample #4 (50-N^+-700) presents a XRD spectrum typical of an anatase polycrystalline network with a preferential orientation according to the (004) plane. Since a similar diagram is also found for as-deposited nonirradiated thin films annealed at 700 K (result not shown), this preferential texturing must be solely attributed to an effect of the temperature during irradiation.

Figure 3(b) shows the N 1*s* photoemission spectra of samples #3 (50-N^+-RT) and #4 (50-N^+-700). In both cases, the spectra are dominated by a main peak at 396.3 eV and a tail extending to higher binding energies that suggests some additional contributions in an energy range going up to 401 eV. Previous studies in literature have attributed different N 1*s* peaks in N-doped TiO_2 to nitride and oxinitride species of the type: Ti-N (396.3 eV), Ti-ON (399.3 eV), and Ti-NO (400.7 eV).[8] According to these previous assignments, the spectra in Fig. 3(b) support the formation of a high concentration of Ti-N species in the implanted samples. Figure 3(c) shows the UV-vis absorption spectra of the as-deposited sample (labeled as REF), along with those of samples #3 (50-N^+-RT) and (50-N^+-700). These spectra depict the typical oscillations caused by the interferences observed when a transparent or partially transparent thin film with high refraction index is deposited on a low refraction index substrate. In addition, the spectra of samples #3 (50-N^+-RT) and #4 (50-N^+-700) evidence a progressive decrease in the transmittance within the whole visible spectral range. Broad absorption features extending from the blue to the red regions of the spectrum have been attributed in literature to N-doped TiO_2 and oxygen-deficient TiO_2, respectively.[31] The comparison between the magnitudes of these absorptions for the two implanted samples indicates that temperature plays an important role in the optical properties of the films inducing an additional loss of transmittance in the sample #4 (50-N^+-700) irradiated at 700 K. This feature agrees with its relatively higher electrical conductivity (see Table I) and suggests a higher reduction degree of this sample. In this regard, since loss of oxygen due to the preferential surface sputtering mechanism mainly affects to the upmost surface layer of the film, migration of oxygen through the whole implantation region must be assumed to compensate this high oxygen concentration gradient from the surface and the formation of a relatively homogeneous $TiO_x(N)$ composition.

Figure 4 reports a series of characterization studies by HAADF-STEM and EELS of sample #3 (50-N^+-RT). Figure 4(b) shows a HAADF image of the cross section of the topmost layers of this sample. Images recorded by this technique offers brightness contrast associated with the concentration and atomic number of constituent elements. Figure 4(b) shows that the topmost surface regions consist of mounds and open pores, with a high density of large voids in the region just below R_p, i.e., below 50 nm, that become smaller in size as we go deeper into the material. These small voids disappear at a depth of about 170 nm, where we find the original columnar structure of the film. Chemical information along this altered layer formed in sample #3 (50-N^+-RT) can be gathered through a sequence of EELS spectra, each taken at a particular position crossing the surface region. Spectra were recorded in spectrum-imaging mode in regularly spaced localizations with 3 nm steps along the vertical arrow displayed in Fig. 4(b), with an acquisition time of 4 s. Nitrogen intensity profiles, extracted from the individual spectra (using the normal background subtraction method[32]) are displayed in Fig. 4(a), whose vertical axis is scaled with Fig. 4(b). This profile shows that a maximum concentration of implanted nitrogen exists at a depth of approximately 100 nm, with a shoulder at around 60 nm. Furthermore, two of these spatially resolved spectra for determined depths (marked by the horizontal arrows) centered in energy range around the N *K* edge are shown in Fig. 4(c), where they have also been scaled in order to compare their shapes. The species of nitrogen at a depth similar to that of the maximum concentration in Fig. 4(a) is characterized by a strong main peak at about 401 eV, which is attributed to molecular nitrogen embedded into the material.[33] In regions closer to the surface (above R_p), corresponding to the region with larger voids in Fig. 4(b), a smaller relative concentration of molecular nitrogen is detected: in this case the N signal is characterized by two peaks at around 398 and 409 eV, indicating the existence of nitride species.[34] This analysis provides evidence that N_2 gas has mostly desorbed from the outer region of the implanted layer whereas it remains trapped in the material below this region. The maximum concentration of nitrogen is found at a depth below R_p, i.e., at about 100 nm from the sample surface, in the region immediately below the largest voids. The nitrogen concentration decreases to disappear for a depth of 170 nm, i.e., at distances from the surface higher than the implantation depth. The electron diffraction patterns (result not shown) indicates that below 170 nm, the film keeps the crystalline planes of anatase whereas for depths above 170 nm, the material is much less crystalline, in agreement with its XRD spectrum depicted in Fig. 3(a).

Figure 5 shows a similar HAADF-STEM and EELS analysis for sample #4 (50-N^+-700). In particular, Fig. 5(b) shows a HAADF-STEM cross-sectional image of the sample, where the existence of surface nanorods, aligned with the direction of the ion beam, and with a length of about 100 nm are clearly visible. In comparison with Fig. 4(a) [sample #3 (50-N^+-RT)], Fig. 5(a) shows a shift in the maximum of the nitrogen depth profile toward the surface. This means that the mobility of N implanted in the material has increased and that thermal diffusion processes have induced a certain migration of nitrogen atoms toward the surface.

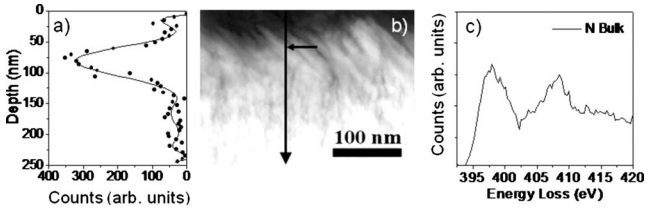

FIG. 5. Chemical analysis of sample #4 (50-N^+-700) in Table I. (a) Nitrogen intensity profiles obtained through the EELS spectra, (b) cross-sectional HAADF image of the surface scaled with part (a), and (c) EELS spectra for the positions given by the horizontal arrows in (b) (slashed and continuum curves correspond to the slashed and continuum arrows).

Furthermore, Fig. 5(b) does not reveal any sign of voids near the surface, indicating that in sample #4 (50-N^+-700) there is a different balance between the mechanisms governing the evolution of the microstructure of the implanted layer. In agreement with that, Fig. 5(c) shows an intense EELS spectrum at the depth indicated by the horizontal arrow, showing two peaks at 398 and 409 eV. Thus, despite the fact that some contribution of molecular nitrogen cannot be discarded, this spectral shape can be reasonably attributed to nitride species.[34] The depth profile in Fig. 5(a) indicates that, just below the nanorods, the amount of nitrogen incorporated to the network increases and reaches a maximum at a depth around 50 nm [i.e., at a depth where large voids were found in Fig. 3(b)]. Then, for deeper zones of the implanted layer, the nitrogen concentration drastically diminishes to practically disappear at around 150 nm. It is also important to mention that electron-diffraction analysis of the implanted region revealed that from the tip of the nanorods to the zone below the implantation region, the whole material possesses an anatase structure with good crystallinity (result not shown). This recrystallization observed in sample #4 (50-N^+-700) must be attributed to the high temperature of the film during irradiation.

C. Surface nanostructuring of irradiated TiO_2

Ion-implantation generated point defects are known to be responsible for the formation of pores under the film surface in different materials. For GaSb irradiated at room temperature with different ions it is known that, in an initial stage, voids of a few nanometres of diameter are formed by the aggregation of migrating vacancies formed as a result of the primary implantation events. This process continues if additionally created vacancies migrate toward the voids, enlarging them or forming new ones, ending up with the formation of spongelike structures at high implantation doses.[25,26] Under low defect mobility conditions (e.g., at low temperatures), vacancies do not aggregate easily and remain scattered in the material. For increasing ion doses under these conditions, it is known that vacancy generation goes on until their concentration reaches a critical value which is typically determined by the elastic properties of the material. At that point, voids are abruptly formed at a depth about the ion projected range. In this way, new vacancies are absorbed by the voids which grow, forming a typical cellular structure.[26,35] In these experiments for GaSb, typical ion doses were between 10^{14} and 10^{15} ions/cm^2 whereas for TiO_2 we found cavities for doses as large as 2.4×10^{17} ions/cm^2, i.e., two-three orders of magnitude above. Interestingly, for both materials similar structures consisting of voids, cellular structures or nanorod surface patterns have been observed. For GaSb irradiated with 30 keV Ga^+ ions, Perez-Bergquist *et al.*[27] found that for low doses (1.3×10^{15} ions/cm^2) the first layers of the material breached, exposing a thin porous regions to the surface. By contrast, at higher doses (6.5×10^{15} ions/cm^2), the pores grew outwards developing a typical nanorod surface pattern. It is also important to stress that for GaSb the mobility of vacancies in the material has a strong dependence on the irradiation temperature, becoming quite important when defining the void formation and growth. Likewise, helium-implanted single-crystal silicon also develops voids whose structural evolution follows a common pattern for increasing doses: for low doses platelike clusters of highly pressurized helium bubbles are formed, whereas for higher doses, helium in these bubbles effuses from the surface leaving empty nanovoids.[21] This evolution has been found to be strongly conditioned by the film temperature, and caused by segregation and precipitation phenomena of helium in the material. The similarities between the abovementioned irradiated materials suggest that similar mechanisms are responsible for the formation of the observed nanostructures in TiO_2. However, we must insist in that in our case a much higher ion dose must be employed in order to achieve the required vacancy concentration.

By considering the previous evidences reported for GaSb,[27] He implanted Si (Ref. 21) and the results presented in this paper for TiO_2, we propose the mechanism schematized in Fig. 6 for the formation of surface patterns in anatase TiO_2. In an initial stage, ions are implanted at a depth about the ion projected range, forming atom vacancies which are scattered in the material. Because of the high dose employed in the irradiation, the defect concentration reaches a critical value and the material collapses forming small voids. It is worthy to mention, that we expect that not only the ion dose but also the ion flux may play a relevant role in the void formation and growth due to the different typical times associated to vacancy formation and migration kinetics in the material. Once voids are formed in the material, they grow in size in a preferential direction defined by the ion beam due to the ion-induced damage in the material (in the same way as explained in Ref. 25 for Sn ion implantation of GaSb thin films). The migration of vacancies and atoms in the material is controlled by the film temperature during irradiation: when the mobility of vacancies in the material is high enough, nearby voids merge, being brought toward the surface due to the sputtering removal of the first layers. This abovementioned nanostructuring processes are responsible for generating a nanorod surface pattern aligned with the angle of incidence of the ion beam as illustrated in Fig. 6. By contrast, when the mobility of single vacancies is low enough, most voids remain isolated from each other, and only a small fraction of them open to the surface. Overall, we have found that high values of the dose and a high temperature enhance the growth of the voids in the material (whenever the ion

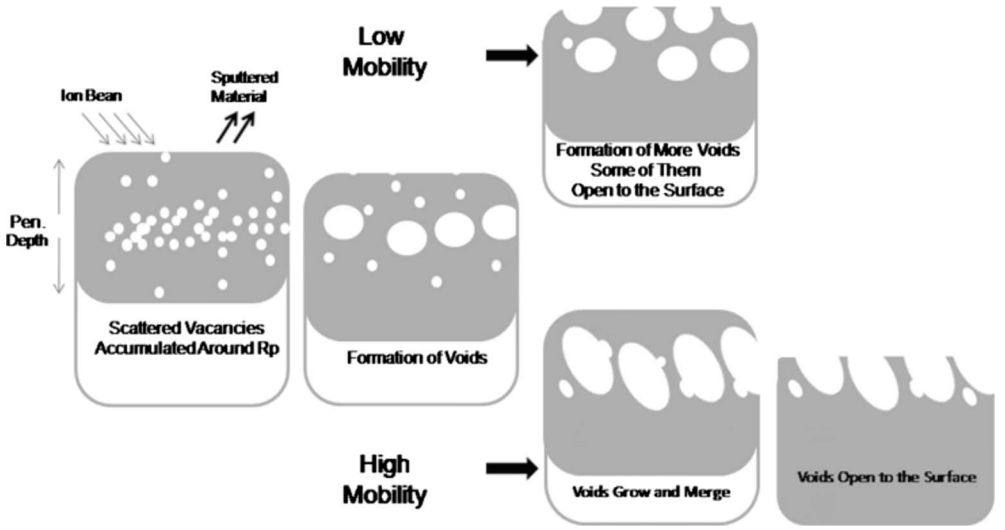

FIG. 6. Proposed model for the void production, growth, coarsening and opening to the surface to explain the different surface nanostructures formed during ion implantation.

dose is high enough to reach the critical density of point defects to make the material collapse). As mentioned above, another important variable is the ion flux: preliminary experiments carried out to check the influence of this quantity have shown that it plays a certain role in determining the formation of voids. However, at the present stage we have not been able to find the critical threshold values of ion dose and flux leading to void formation.

In our model, a key parameter is the mobility of the vacancies in the partially reduced titanium oxide. This mobility is enhanced by the fact that the implanted region consists of a defective TiO_x(N) material with a significant loss of stoichiometry due to the preferential release by sputtering of oxygen from the topmost surface layers and the thermally activated migration of oxygen toward the surface responsible for the homogeneization of the oxygen concentration in the implanted region. In fact, Rutherford backscattering spectroscopy characterization of the implanted layers shows an excess of Ti over the TiO_2 stoichiometry (result not shown). Defective titanium oxides are known for having a high lattice mobility and structural plasticity (a typical case is that of the so-called Magnelli phases, well known for their easy rearrangement at moderate temperatures[36]), a feature that must be the main factor responsible for the surface nanostructuring processes undergone by the implanted and heated samples. Thus, film temperature during irradiation governs two cumulative processes that contribute to void growth: on the one hand film temperature directly controls the atoms and vacancies mobility in the network, and, on the other hand, it also contributes to homogenize the oxygen concentration in the implanted region, a feature that also enhances to the overall mobility in the material.

D. General character of the surface patterning processes with other ions

Vacancy formation and loss of stoichiometry during ion implantation must depend not only on temperature but also on the reactivity of the implanted ion species. To check to which extent the basic guidelines of the model in Fig. 6 comply with the results, we have carried out equivalent irradiations using F^+ and S^+ as implantation ions. In comparison with N and O, F and S atoms cannot be released so easily in the form of gaseous molecules and it can be expected that they will become incorporated more efficiently to the TiO_x network. This means that their use as irradiation ions should favor the removal of point defects and lower down their production rate. Figure 7 shows the SEM micrographs corresponding to samples #5 (50-F^+-RT), #6 (50-F^+-700) and #7 (50-S^+-700). Figure 7(a) shows the cross-sectional view of sample #5 (50-F^+-RT) irradiated at room temperature. Since no trace of voids is appreciable in the image, we can conclude that either they do not form under the used irradiation conditions or they are too small to be detected. Furthermore, the surface electrical resistivity of this sample (see values in Table I) is higher than that for samples #3 (50-N^+-RT) and #4 (50-N^+-700), thus suggesting a lower defect concentration in the fluorine implanted region. By contrast, if the ion irradiation takes place at 700 K we found a different behavior as evidenced by the normal view SEM micrograph in Fig. 7(b)

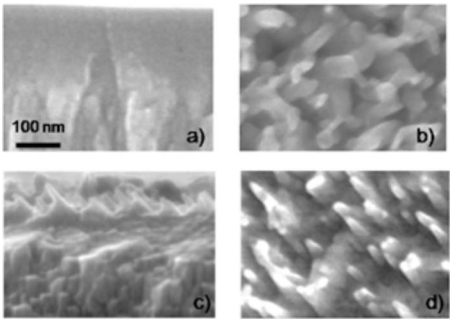

FIG. 7. SEM micrographs of TiO_2 anatase thin films: (a) cross-sectional view of sample #5 (50-F^+-RT) in Table I, (b) top view of sample #6 (50-F^+-700), (c) cross-sectional view of sample #7 (50-S^+-700), and (d) top view of sample #7 (50-S^+-700).

showing that the microstructure of this sample is similar to that of sample #4 (50-N^+-700).

The above-mentioned results suggest that, at room temperature, the growth of voids is completely inhibited due to the low mobility and/or low production rate of point defects, caused by the incorporation of fluorine to the material's network. However, the increase in the implantation temperature up to 700 K enhances the mobility of the vacancies and atoms in the material contributing to the migration of oxygen and therefore to the survival of point defects not saturated by fluorine. This is corroborated by the value of the resistivity of the film, which by increasing several orders of magnitude [see results for sample #6 (50-F^+-700) in Table I] indicates a significant loss of stoichiometry and the accumulation of defects in the implanted layer. This highly defective surface state evolves toward the development of a surface pattern as that schematized by the low mobility case in Fig. 6. According to our model, an even higher substrate temperature would be necessary in order to enhance the surface mobility required to generate a nanorod surface pattern. Unfortunately, experimental limitations in our setup impeded us to verify this model hypothesis.

To confirm the general character of the aforementioned phenomena and, therefore, support the premises of our model, TiO_2 thin films have been irradiated with less electronegative species under the assumption that they will present a lesser tendency than O, N, or F to become incorporated into the material's network. The corresponding experiment consisted of the irradiation with a half ion dose of S^+ ions, the other conditions remaining similar to those used for sample #4 (50-N^+-700). The lower dose used in this experiment is intended to limit the magnitude of the network damage induced by this higher atomic mass ion. Even though, the cross-sectional and top view SEM micrographs of sample #7 (50-S^+-700) reported in Figs. 7(c) and 7(d) show that the open voids appearing at the surface are deformed in the direction of the ion beam and become open to the surface shaping a structure consisting of ellipsoidal voids and tilted nanorods. The resistivity measurements for this sample reported in Table I show that it is more conductive than sample #4 (50-N^+-700), probably because it contains a larger number of defects and vacancies in its structure. All these features agree with the formation of a surface pattern as that schematized by the high mobility cartoon in Fig. 6. The previous results confirm that the formation of surface nanorods in irradiated TiO_2 thin films can be achieved by using a wide variety of ions and experimental conditions (ion dose and temperature) provided that a critical concentration of oxygen vacancies is reached in the implanted layer.

IV. CONCLUSIONS

In this paper, we have discussed the effects of a high ion dose irradiation on TiO_2 thin films under different conditions of temperature and ion nature. We have found three different microstructures depending on the type of ion and the degree of mobility in the network, this latter depending on temperature and the degree of nonstoichiometry of the implanted samples. We have shown that at room temperature N^+ irradiated TiO_2 anatase thin films develop a typical microstructure with mounds and voids open to the surface. Meanwhile, irradiations at 700 K generate a surface pattern consisting of ordered nanorods aligned with the ion beam. The formation of these patterns is caused by the simultaneous effect of ion irradiation and film temperature that favors the structural mobilization of the defective lattice of the irradiated titanium oxide. A qualitative model has been proposed to account for the void formation, their growth and merging within the ion penetration depth, as well as their opening toward the surface. This model takes into account the generation of ion-induced point defects and the mobility and the coarsening of the vacancies in the material. The general character of these phenomena has been tested by using F^+ ions as projectiles. With these experiments, we have shown that temperature plays a crucial role during irradiation finding an almost flat surface at low temperatures and a porous surface pattern at 700 K. A similar experiment with S^+ ions confirm that the reported procedure can be considered as a common method for the surface nanostructuring of TiO_2 anatase thin films. Finally, our results confirm the validity of the ion irradiation methodology for the production of tilted nanorod patterns that depend on the irradiation beam characteristics. This technique may have a great impact for multiple applications and, very likely, for the surface nanostructuring of other materials with different functionalities.

ACKNOWLEDGMENTS

Financial support from the Spanish Ministry of Innovation (Projects No. MAT 2007-65764, CONSOLIDER INGENIO No. 2010-CSD2008-00023, and PIE No. 200960I132) and the Junta de Andalucía (Projects No. TEP2275 and No. P07-FQM-03298) is acknowledged. We would also like to acknowledge a grant of the EU to carry out the implantation experiments in the Forschungzentrum of Rossendorf (Germany).

*alberto.palmero@icmse.csic.es

[1] O. Carp, C. L. Huisman, A. Reller, Prog. Solid State Chem. **32**, 33 (2004).

[2] A. Fujishima, T. N. Rao, and D. A. Tryk, J. Photochem. Photobiol. C **1**, 1 (2000).

[3] M. R. Hoffmann, S. T. Martin, D. W. Choi, and D. W. Bahnemann, Chem. Rev. **95**, 69 (1995).

[4] M. Fujihira, Y. Satoh, and T. Osa, Nature (London) **293**, 206 (1981).

[5] U. Diebold, Surf. Sci. Rep. **48**, 53 (2003).

[6] V. Rico, P. Romero, J. L. Hueso, J. P. Espinós, and A. R. González-Elipe, Catal. Today **143**, 347 (2009).

[7] R. Asahi, T. Morikawa, T. Ohwaki, K. Aoki, and Y. Taga, Science **293**, 269 (2001).
[8] P. Romero-Gómez, V. Rico, A. Borrás, A. Barranco, J. P. Espinós, J. Cotrino, and A. R. González-Elipe, J. Phys. Chem. C **113**, 13341 (2009).
[9] D. V. Bavykin, J. M. Friedrich, and F. C. Walsh, Adv. Mater. **18**, 2807 (2006).
[10] M. Zukalová, A. Zukal, L. Kavan, M. K. Nazeeruddin, P. Liska, and M. Grätzel, Nano Lett. **5**, 1789 (2005).
[11] M. Adachi, Y. Murata, J. Takao, J. Jiu, M. Sakamoto, and F. Wang, J. Am. Chem. Soc. **126**, 14943 (2004).
[12] M. Law, L. E. Greene, J. C. Johnson, R. Saykally, and P. D. Yang, Nature Mater. **4**, 455 (2005).
[13] M. Paulose, O. K. Varghese, G. K. Mor, C. A. Grimes, and K. G. Ong, Nanotechnology **17**, 398 (2006).
[14] G. K. Mor, K. Shankar, M. Paulose, O. K. Varghese, and C. A. Grimes, Nano Lett. **6**, 215 (2006).
[15] K. Shankar, G. K. Mor, H. E. Prakasam, S. Yoriya, M. Paulose, O. K. Varghese, and C. A. Grimes, Nanotechnology **18**, 065707 (2007).
[16] C. A. Grimes, J. Mater. Chem. **17**, 1451 (2007).
[17] P. Romero-Gomez, A. Palmero, F. Yubero, M. Vinnichenko, A. Kolitsch, and A. R. Gonzalez-Elipe, Scr. Mater. **60**, 574 (2009).
[18] S. Nakao, T. Nonami, P. Jin, Y. Miyagawa, and S. Miyagawa, Surf. Coat. Technol. **128-129**, 446 (2000).
[19] T.-H. Her, R. J. Finlay, C. Wu, and S. Deliwala, Appl. Phys. Lett. **73**, 1673 (1998).
[20] M. Shen, J. E. Carey, C. H. Crouch, M. Kandyla, H. A. Stone, and E. Mazur, Nano Lett. **8**(7), 2087 (2008).
[21] S. Frabboni, F. Corni, C. Nobili, R. Tonini, and G. Ottaviani, Phys. Rev. B **69**, 165209 (2004).
[22] S. O. Kucheyev, J. S. Williams, C. Jagadish, J. Zhou, V. S. J. Craig, and G. Li, Appl. Phys. Lett. **77**, 1455 (2000).
[23] S. O. Kucheyev, J. S. Williams, J. Zhou, C. Jagadish, and G. Li, Appl. Phys. Lett. **77**, 3577 (2000).
[24] S. O Kucheyev, J. E. Bradby, C. P. Li, S. Ruffell, T. van Buuren, and T. E. Felter, Appl. Phys. Lett. **91**, 261905 (2007).
[25] N. Nitta, M. Taniwaki, Y. Hayashi, and T. Yoshiie, J. Appl. Phys. **92**, 1799 (2002).
[26] N. Nitta, M. Taniwaki, Y. Hayashi, and T. Yoshiie, Physica B **376-377**, 881 (2006).
[27] A. Perez-Bergquist, S. Zhu, Kai Sun, X. Xiang, Y. Zhang, and L. Wang, Small **4**, 1119 (2008).
[28] A. Borras, C. Lopez, V. Rico, F. Gracia, and A. R. Gonzalez-Elipe, J. Phys. Chem. C **111**, 1801 (2007).
[29] http://www.srim.org/
[30] T. Le Mercier, J.-M. Mariot, P. Parent, M.-F. Fontaine, C. F. Hague, and M. Quarton, Appl. Surf. Sci. **86**, 382 (1995).
[31] Z. Lin, A. Orlov, R. M. Lambert, and M. C. Oayne, J. Phys. Chem. B **109**, 20948 (2005).
[32] R. F. Egerton, *Electron Energy-Loss Spectroscopy in the Electron Microscope* (Plenum Press, New York, 1996), p. 245.
[33] R. McLaren, S. A. C. Clark, I. Ishii, and A. P. Hitchcock, Phys. Rev. A **36**, 1683 (1987).
[34] S. Trasobares, O. Stephan, C. Colliex, G. Hug, W. K. Hsu, H. W. Kroto, and D. R. M. Walton, Eur. Phys. J. B **22**, 117 (2001).
[35] F. H. Eisen, Phys. Rev. **123**, 736 (1961).
[36] L. Liborio and N. Harrison, Phys. Rev. B **77**, 104104 (2008).